ACS Photonics

pubs.acs.org/journal/apchd5

Letter

On-Chip Notch Filter on a Silicon Nitride Ring Resonator for Brillouin Spectroscopy

Giuseppe Antonacci,* Kareem Elsayad, and Dario Polli

Cite This: *ACS Photonics* 2022, 9, 772−777

Read Online

ACCESS | Metrics & More | Article Recommendations | Supporting Information

ABSTRACT: Noncontact Brillouin spectroscopy is a purely optical and label-free method to retrieve fundamental material viscoelastic properties. Recently, the extension to a three-dimensional imaging modality has paved the way to novel exciting opportunities in the biomedical field, yet the detection of the Brillouin spectrum remains challenging as a consequence of the dominant elastic background light that typically overwhelms the inelastic Brillouin peaks. In this Letter, we demonstrate a fully integrated and ultracompact notch filter based on an optical ring resonator fabricated on a silicon nitride platform. Our on-chip ring resonator filter was measured to have a ∼10 dB extinction ratio and a Q factor of ∼1.9 × 10^5 at 532 nm central wavelength. The experimental results provide a proof-of-concept on the ability of the on-chip filter to attenuate the elastic background light, heralding future developments of fully integrated, ultracompact, and cost-effective Brillouin spectrometers.

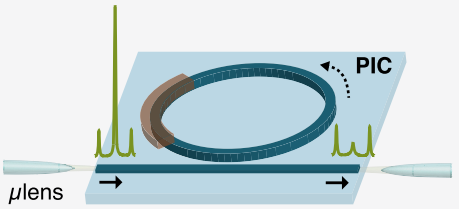

KEYWORDS: *silicon photonics, silicon nitride, photonics integrated circuits, Brillouin spectroscopy*

Noncontact Brillouin spectroscopy optically provides access to the elastic moduli forming the full material elastic tensor.[1−3] Combination of this method with confocal microscopy[4,5] has enabled a wide variety of applications in the life sciences and mechanobiology including the elasticity assessment of the ocular lens and cornea *in vivo*,[6] the 3D mechanical imaging of living cells,[7−10] as well as the investigation of the liquid-to-solid phase transitions of intracellular compartments.[11−13] Moreover, Brillouin spectroscopy holds promises to become a diagnostic tool in clinical environments,[14] where altered biomechanical properties are understood to be the primary initiators of age-linked pathologies such as keratoconus,[15] cancer,[16,17] and atherosclerosis.[18]

Despite the broad range of potential applications,[19] Brillouin spectroscopy remains challenging in the spontaneous regime as a consequence of the dominant elastic background light arising from both Rayleigh scattering and specular reflections. When the relative strength difference between the elastic and inelastic spectral components exceeds the contrast of the spectrometer, the Brillouin peaks are overwhelmed and cannot be detected. Multipass Fabry−Perot interferometers of high (∼10^{15}) spectral contrast have for long been used in Brillouin spectroscopy,[20] but their relative slow scanning process imposes a long (typically >1 s) data acquisition time that makes them not suitable for 3D imaging. To overcome this limit, a modified nonscanning version of the solid Fabry−Perot etalon, namely, a Virtually Imaged Phased Array (VIPA), has been used in Brillouin microscopy.[21] Yet, its limited (∼30 dB) spectral contrast imposes complex multistage architectures that affect the system throughput efficiency and increase complexity. Extensive research has been carried out both to increase the spectral contrast of VIPA-based spectrometers and to suppress the unwanted elastic background light. Beam apodization has been used to equalize the exponentially decaying beam at the output of the VIPA using linear absorption filters[7] and spatial light modulators.[22] Other successful methods for spectral contrast enhancement involved the use of diffraction masks[11] and Lyot filters.[23] On the other hand, suppression methods involved the use of absorption cells,[24] dark-field illumination with annular beams,[25] and interferometric schemes.[26−29] While these methods offer a spectral visibility gain in the order of 30−40 dB, they rely on bulk optical components that generally affect the system robustness and increase complexity. Moreover, free-space filters are particularly sensitive to environmental temperature variations and mechanical drifts affecting the optical path length and therefore the system stability.

In this Letter, we demonstrate an integrated microring resonator working as a notch filter to suppress the elastic background light. A ring resonator is a resonant cavity integrated on a Silicon Photonics chip where the resonance condition occurs when the optical length of the ring is exactly an integer number *m* of the central wavelength (Figure 1a).[30] High Q factor ring resonators have been extensively used for a broad range of applications including datacom[31] and sensing.[32]

Received: January 4, 2022
Published: February 23, 2022

https://doi.org/10.1021/acsphotonics.2c00005
ACS Photonics 2022, 9, 772−777

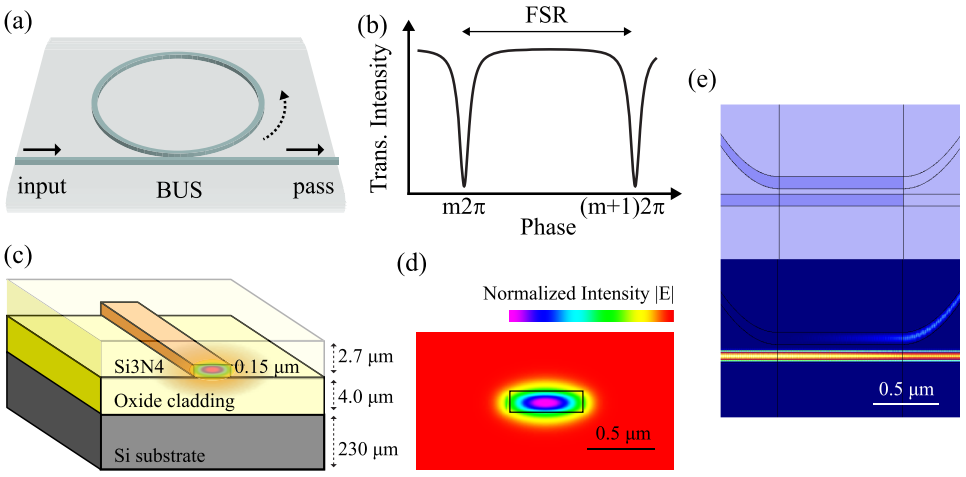

Figure 1. All-pass ring resonator (a). Light is coupled to the ring from a BUS waveguide. The transmission intensity profile at the pass port of the ring exhibits sharp periodic dips at the ring resonances occurring at each 2π roundtrip phase shift (b). PIC structure (c). The Si_3N_4 waveguides of $0.15 \times 0.60\ \mu m^2$ are embedded in a SiO_2 cladding, providing tight confinement of the fundamental TE mode (d). Simulation of the ring coupling in a racetrack configuration (e).

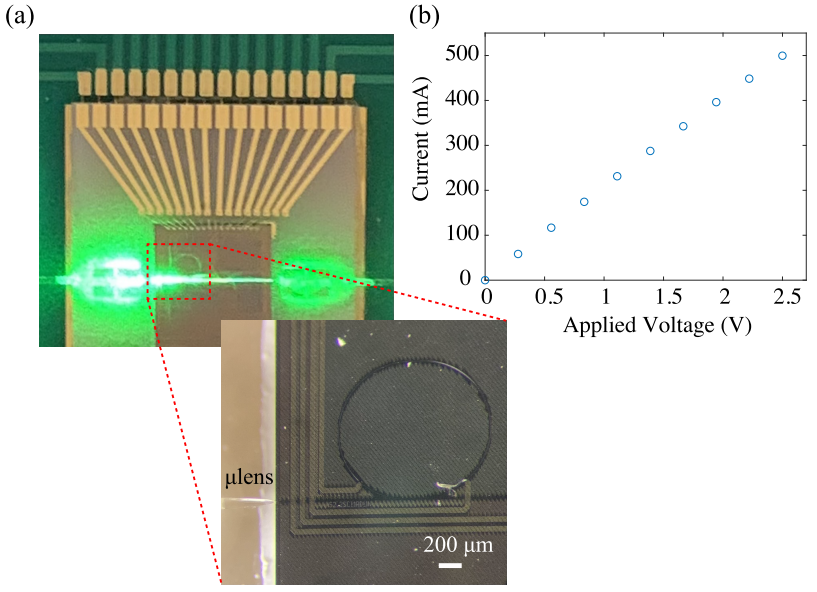

Figure 2. Functional PIC assembly (a). The optical coupling was achieved using microlensed single-mode fibers that partially mitigated the MFD mismatch with the Si_3N_4 waveguides. The PIC was mounted on a PCB to ease electrical accessibility. Current plot as a function of the applied voltage, indicating a ring heather resistance of ~5 Ω (b).

The recent development of the high index contrast silicon nitride (Si_3N_4) platform has extended the use of Photonics Integrated Circuits (PICs) in the visible range,[33] in turn heralding opportunities in fields such as spectroscopy,[34] sensing,[35] and microscopy.[36] We exploited the Si_3N_4 platform to design and fabricate a narrowband ring-based notch filter for operation at λ = 532 nm central wavelength. The ring was conceived in an all-pass mode so as to provide a similar transfer function to that of a Fabry−Perot interferometer working in reflection, namely, an almost flat transmission intensity with narrow dips occurring at the ring resonance and equally spaced in frequency (Figure 1b). The frequency separation of two consecutive resonance peaks is defined by the Free Spectral Range (FSR) given by the expression

$$\mathrm{FSR} = \frac{\lambda^2}{n_g L} \tag{1}$$

where n_g is the group index and L the ring roundtrip length (Figure 1b). From eq 1 and an estimated group index of n_g = 2.153 (Supporting Figure S1), we set a ring radius of R = 565 μm to have a FSR = 40 GHz. The PIC was fabricated through a low pressure chemical vapor deposition (LPCVD) process for an accurate deposition of the silicon oxide and silicon nitride layers. A representative layout of the PIC layer structure is shown in Figure 1c. The resulting Si_3N_4 waveguides had a nominal dimension of x = 0.60 μm and y = 0.15 μm to ensure a tight confinement of the fundamental TE mode and thus to minimize the bending losses. Figure 1d shows the simulated TE mode with respect to the Si_3N_4 waveguide. To finely tune the resonant wavelengths of the ring, a phase shifter is needed to change the effective refractive index n_{eff} of the ring waveguide. In the present study, a 2π phase shift was achieved by locally heating the Si_3N_4 waveguide of the ring through the application of an electrical current to a metal resistor placed

https://doi.org/10.1021/acsphotonics.2c00005
ACS Photonics 2022, 9, 772−777

above the ring. Since metal could increase the propagation loss and thus affect both the extinction ratio and the Q factor, numerical simulations have been performed to ensure that the upper cladding thickness was sufficient to avoid extra absorption loss inside the ring caused by the metal resistor (Supporting Figure S2). To maximize the extinction ratio of the filter, the ring was designed in an attempt to achieve a critical coupling, a condition that occurs when the coupled power equals the power loss in the ring. Assuming an estimated loss coefficient of α = 1 dB/cm, this condition was simulated to be satisfied for a ring coupling power efficiency of k = 12.2%. To this aim, the ring was designed with a gap size of 275 nm and a racetrack configuration, i.e., with an elongated shape of 93.86 μm along the direction of the BUS waveguide (Figure 1e). The racetrack configuration was needed to compensate for the tight confinement of the evanescent field across the waveguides and the minimum gap size imposed by the fab resolution in an attempt to achieve the target coupling power. Numerical simulations have been performed to evaluate the ring coupling power k as a function of both gap size and racetrack coupling length (Supporting Figure S3).

To functionalize the filter, the PIC was packaged so as to provide both electrical and optical coupling (Figure 2a). To ease the electrical accessibility needed for the thermal tuning, the PIC was mounted and wire bonded on a custom printed circuit board (PCB), whose inputs and outputs were connected to a current supplier (Keysight E36312A). Preliminary tests were conducted to verify the electrical conductivity of the heaters and its resistance by reading the circuit current in response to an applied voltage (Figure 2b). Given the mode field diameter (MFD) mismatch between a conventional single-mode fiber for visible light (MFD ~ 4 μm) and our Si_3N_4 waveguides (MFD_x ~ 0.50 μm, MFD_y ~ 0.27 μm), a direct fiber-to-chip coupling would result in high (>40 dB) insertion losses that may prevent the detection of the Brillouin signal. To overcome this limitation, we employed two lensed single-mode fibers (Thorlabs SM450) of NA ~ 0.4 and nominal MFD = 0.8 μm in an attempt to limit the optical insertion loss, which we measured to be ~18 dB per facet. Although around 5 dB insertion loss per facet may be achieved in principle with the present configuration,[37] we obtained higher loss as a consequence of the challenging alignment process given by the nm accuracy requirement as well as the micromechanical drifts arising during the epoxy curing process.

We measured the extinction ratio of our on-chip ring filter by coupling the monochromatic light of a narrowband single longitudinal mode laser with high spectral purity (Laser Quantum torus, λ = 532 nm) directly to the PIC and finely tuning the ring for two consecutive interference orders, i.e., for a round trip phase change of 2π. The spectral profile was then reconstructed by measuring the light signal transmitted trough the pass port of the ring at the output of the lensed single-mode fiber. Figure 3 shows the resulting spectral profile of the ring for two consecutive resonances. By fitting the peaks with a Lorentzian function, we measured an extinction ratio of ~9.7 dB, a finesse $F = FSR/\delta\nu$ ~ 13.3, and a peak line width of $\delta\nu$ ~ 3 GHz, indicating a Q factor of $Q = \nu/\delta\nu$ ~ 1.9 × 10^5 and a loss coefficient α ~ 1.3 dB/cm, in line with our expectations. Table 1 provides a comparison with other previously demonstrated Si_3N_4 ring and microdisk resonators in the visible and NIR range.

Although ring resonators with a Q factor higher than a million have been obtained, we shall note that this is partially due to the typically lower surface scattering at longer wavelengths that significantly contributes to the total waveguide propagation loss.

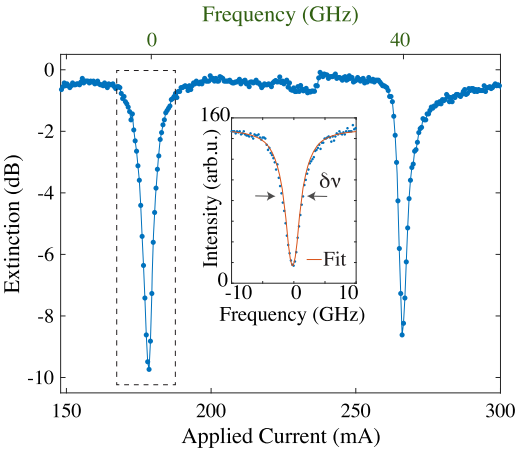

Figure 3. Spectral profile (in dB units) of the ring resonator for monochromatic (λ = 532 nm) light and for two consecutive ring resonances as a function of both frequency (top axis) and applied current (bottom axis). Resonant peak profile (in linear scale) and associated Lorentzian fit as a function of frequency (inset). Data show an extinction ratio of 9.7 dB and a peak line width of $\delta\nu$ = 3.0 GHz, corresponding to a ring Q factor of 1.9 × 10^5.

Table 1. Comparison between Ring and Microdisk Resonators at Visible and NIR Wavelengths

λ (nm)	radius (μm)	extinction (dB)	Q factor	reference
532	565	~10	1.9 × 10^5	present study
660	20	~3	6 × 10^5	E. S. Hosseini et al.[38]
668	25	~6	1.5 × 10^5	X. Lu et al.[39]
780	20	~2	1.5 × 10^4	C. Doolin et al.[40]
780	300	~5	1.4 × 10^6	M. Sinclair et al.[41]
784	350	~0.5	3.6 × 10^6	L. Stefan et al.[42]

A Brillouin optical system (Figure 4a) was built in a 90° scattering geometry to provide a proof-of-concept experiment of the capability of the on-chip ring filter to suppress the elastic background light in Brillouin spectral measurements. The laser beam was first coupled into a single-mode fiber for mode cleaning and then focused to a polystyrene cuboid of transparent and polished facets that was used as a test sample. The scattered light was collected at 90° by a lens of equal NA = 0.2 with respect to the illumination one and delivered to our on-chip filter through the assembled fiber, which also acted as a confocal pinhole at the collection arm. The output fiber of the PIC was then connected to a single-stage VIPA spectrometer integrating a VIPA etalon (LightMachinery) of FSR = 60 GHz, a diffraction mask for spectral contrast enhancement,[11] and a CCD camera (FLIR BFS-U3-63S4M-C).

Figure 4b shows the Brillouin spectrum of the polystyrene test sample acquired by the VIPA spectrometer before and after tuning the ring resonance at the laser wavelength. Given the relatively high optical insertion loss at the PIC input and output waveguides, we set an illumination power of ~150 mW at the sample plane and a data acquisition time of 30 s averaging over 5 repetitions. With the ring off resonance, the Brillouin peaks were almost completely dominated by the elastic crosstalk light arising from the amorphous structure of polystyrene. In turn, the visibility of the Brillouin peaks

https://doi.org/10.1021/acsphotonics.2c00005
ACS Photonics 2022, 9, 772−777

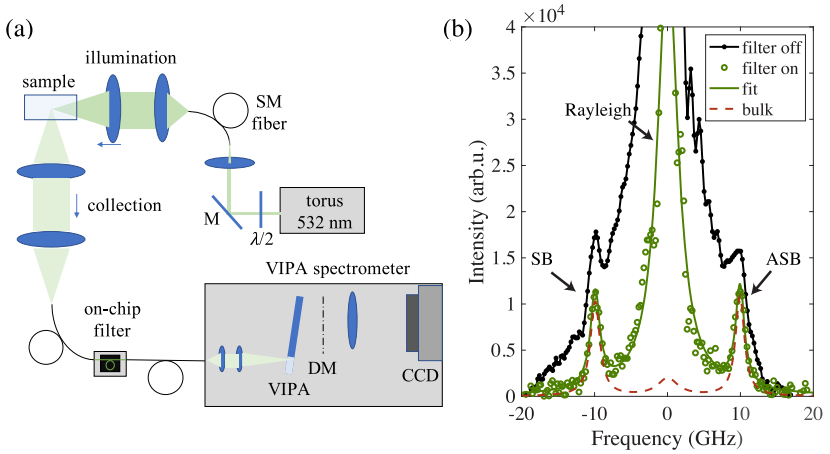

Figure 4. Brillouin spectroscopy platform (a). The laser beam was coupled into a single-mode fiber (SM fiber) and focused to the sample. The light scattered is collected at 90° by a single-mode fiber working as a confocal pinhole and coupled to the on-chip filter for elastic background cleaning. The output fiber of the filter is then connected to a single-stage VIPA spectrometer for parallel spectral acquisition. A CCD camera is used to detect the Stokes (SB) and Anti-Stokes (ASB) Brillouin peaks of polystyrene with the filter turned on and off (b). Red dashed line gives a qualitative comparison with a representative spectrum that would be obtained using existing bulk filters. $\lambda/2$, half wave plate; M, mirror; DM, diffraction mask.

increased significantly as the ring resonance was finely tuned at the laser wavelength. Fitting the Brillouin peaks with a Lorentzian function, we measured a Brillouin shift of ν_B = 9.9 GHz and the acoustic velocity V = 2330m/s, in good agreement with the expected values for polystyrene.[43]

In conclusion, we demonstrated a fully integrated on-chip notch filter for Brillouin spectroscopy based on a racetrack all-pass ring resonator fabricated on a silicon nitride platform. While racetrack ring resonators are common components in integrated photonics, their application as notch filters for Brillouin spectroscopy in the visible domain represents a key cornerstone in an attempt of eliminating the need for free-space optics and developing ultracompact and miniaturized systems. Although the measured extinction ratio achieved in the present study is not yet comparable with the 30 dB typically obtained by standard Brillouin bulk filters, our integrated notch filter provides unprecedented robustness, ease-of-use, and stability as neither free-space optical components nor moving parts are needed. Ultimately, this gives the opportunity to reduce the system volume down to a few cubic centimeters, i.e., by at least 2 orders of magnitude compared to existing bulk filters with minimal extra power consumption.

Higher extinction may be reached depending on the level of balance between the ring coupling power and the roundtrip loss. Nevertheless, an exact knowledge of the coupling as a function of the ring gap size and racetrack length is nontrivial as a consequence of the fabrication tolerances and typically requires multiple fabrication runs. On the other hand, higher extinction ratios may also be achieved by cascading multiple ring resonators in tandem with no significant increase in the system footprint, complexity, nor insertion loss. Besides the increase in the extinction ratio, future implementations will also involve a significant reduction in the PIC insertion loss, which may extend the applicability of the on-chip notch filter to Brillouin microscopy where a high throughput efficiency is needed to enable a fast (<100 ms) data acquisition with minimal (<10 mW) optical power for probing living biological systems. Results pave the way to further development of on-chip notch filters not only for Brillouin spectroscopy, but also for the other spectroscopy methods working with visible light such as low-frequency Raman. Last but not least, improvements in the ring Q factor at visible wavelengths may also inspire future implementations of ultracompact and cost-effective spectrometers.

■ ASSOCIATED CONTENT

Supporting Information

The Supporting Information is available free of charge at https://pubs.acs.org/doi/10.1021/acsphotonics.2c00005.

Additional numerical simulations on system design including waveguide group index, absorption loss, and coupling power (PDF)

■ AUTHOR INFORMATION

Corresponding Author

Giuseppe Antonacci − *Specto Srl, 20123 Milan, Italy;* orcid.org/0000-0001-5788-4853; Email: giuseppe@spectophotonics.com

Authors

Kareem Elsayad − *Division of Anatomy, Center for Anatomy and Cell Biology, Medical University of Vienna, Vienna A-1090, Austria*

Dario Polli − *Specto Srl, 20123 Milan, Italy; Dipartimento di Fisica, Politecnico di Milano, 20133 Milan, Italy;* orcid.org/0000-0002-6960-5708

Complete contact information is available at: https://pubs.acs.org/10.1021/acsphotonics.2c00005

Notes

The authors declare the following competing financial interest(s): Giuseppe Antonacci and Dario Polli own shares of Specto Srl.

■ ACKNOWLEDGMENTS

We thank Dr. Gregor Klatt and Laser Quantum—A Novanta Company for a free loan of the *torus* SLM laser.

REFERENCES

(1) Prevedel, R.; Diz-Muñoz, A.; Ruocco, G.; Antonacci, G. Brillouin microscopy: an emerging tool for mechanobiology. *Nat. Methods* **2019**, *16*, 969−977.
(2) Koski, K. J.; Akhenblit, P.; McKiernan, K.; Yarger, J. L. Non-invasive determination of the complete elastic moduli of spider silks. *Nat. Mater.* **2013**, *12*, 262−267.
(3) Palombo, F.; Fioretto, D. Brillouin light scattering: applications in biomedical sciences. *Chem. Rev.* **2019**, *119*, 7833−7847.
(4) Koski, K.; Yarger, J. Brillouin imaging. *Appl. Phys. Lett.* **2005**, *87*, 061903.
(5) Scarcelli, G.; Yun, S. H. Confocal Brillouin microscopy for three-dimensional mechanical imaging. *Nat. Photonics* **2008**, *2*, 39.
(6) Scarcelli, G.; Yun, S. H. In vivo Brillouin optical microscopy of the human eye. *Opt. Express* **2012**, *20*, 9197−9202.
(7) Scarcelli, G.; Polacheck, W. J.; Nia, H. T.; Patel, K.; Grodzinsky, A. J.; Kamm, R. D.; Yun, S. H. Noncontact three-dimensional mapping of intracellular hydromechanical properties by Brillouin microscopy. *Nat. Methods* **2015**, *12*, 1132.
(8) Antonacci, G.; Braakman, S. Biomechanics of subcellular structures by non-invasive Brillouin microscopy. *Sci. Rep.* **2016**, *6*, 37217.
(9) Elsayad, K.; Werner, S.; Gallemi, M.; Kong, J.; Sanchez Guajardo, E. R.; Zhang, L.; Jaillais, Y.; Greb, T.; Belkhadir, Y. Mapping the subcellular mechanical properties of live cells in tissues with fluorescence emission−Brillouin imaging. *Sci. Signal.* **2016**, *9*, rs5.
(10) Coppola, S.; Schmidt, T.; Ruocco, G.; Antonacci, G. Quantifying cellular forces and biomechanical properties by correlative micropillar traction force and Brillouin microscopy. *Biomedical Opt. Express* **2019**, *10*, 2202−2212.
(11) Antonacci, G.; de Turris, V.; Rosa, A.; Ruocco, G. Background-deflection Brillouin microscopy reveals altered biomechanics of intracellular stress granules by ALS protein FUS. *Commun. Biol.* **2018**, *1*, 139.
(12) Schlüßler, R.; Kim, K.; Nötzel, M.; Taubenberger, A.; Abuhattum, S.; Beck, T.; Müller, P.; Maharana, S.; Cojoc, G.; Girardo, S.; Hermann, A.; Alberti, S.; Guck, J. Correlative all-optical quantification of mass density and mechanics of sub-cellular compartments with fluorescence specificity. *eLife* **2022**, *11*, No. e68490.
(13) De Santis, R.; Alfano, V.; de Turris, V.; Colantoni, A.; Santini, L.; Garone, M. G.; Antonacci, G.; Peruzzi, G.; Sudria-Lopez, E.; Wyler, E.; Anink, J. J.; Aronica, E.; Landthaler, M.; Pasterkamp, R. J.; Bozzoni, I.; Rosa, A. Mutant FUS and ELAVL4 (HuD) Aberrant Crosstalk in Amyotrophic Lateral Sclerosis. *Cell Rep.* **2019**, *27*, 3818−3831.
(14) Rioboó, R. J. J.; Gontán, N.; Sanderson, D.; Desco, M.; Gómez-Gaviro, M. V. Brillouin Spectroscopy: From Biomedical Research to New Generation Pathology Diagnosis. *Int. J. Mol. Sci.* **2021**, *22*, 8055.
(15) Scarcelli, G.; Besner, S.; Pineda, R.; Yun, S. H. Biomechanical characterization of keratoconus corneas ex vivo with Brillouin microscopy. *Invest. Ophthalmol. Visual Sci.* **2014**, *55*, 4490−4495.
(16) Margueritat, J.; Virgone-Carlotta, A.; Monnier, S.; Delanoe-Ayari, H.; Mertani, H. C.; Berthelot, A.; Martinet, Q.; Dagany, X.; Riviere, C.; Rieu, J.-P.; Dehoux, T. High-frequency mechanical properties of tumors measured by Brillouin light scattering. *Phys. Rev. Lett.* **2019**, *122*, 018101.
(17) Troyanova-Wood, M.; Meng, Z.; Yakovlev, V. V. Differentiating melanoma and healthy tissues based on elasticity-specific Brillouin microspectroscopy. *Biomedical Opt. Express* **2019**, *10*, 1774−1781.
(18) Antonacci, G.; Pedrigi, R. M.; Kondiboyina, A.; Mehta, V. V.; De Silva, R.; Paterson, C.; Krams, R.; Török, P. Quantification of plaque stiffness by Brillouin microscopy in experimental thin cap fibroatheroma. *J. R. Soc., Interface* **2015**, *12*, 20150843.
(19) Antonacci, G.; Beck, T.; Bilenca, A.; Czarske, J.; Elsayad, K.; Guck, J.; Kim, K.; Krug, B.; Palombo, F.; Prevedel, R.; Scarcelli, G. Recent progress and current opinions in Brillouin microscopy for life science applications. *Biophys. Rev.* **2020**, *12*, 615−624.
(20) Scarponi, F.; Mattana, S.; Corezzi, S.; Caponi, S.; Comez, L.; Sassi, P.; Morresi, A.; Paolantoni, M.; Urbanelli, L.; Emiliani, C.; Roscini, L.; Corte, L.; Cardinali, G.; Palombo, F.; Sandercock, J. R.; Fioretto, D. High-performance versatile setup for simultaneous Brillouin-Raman microspectroscopy. *Phys. Rev. X* **2017**, *7*, 031015.
(21) Scarcelli, G.; Yun, S. H. Multistage VIPA etalons for high-extinction parallel Brillouin spectroscopy. *Opt. Express* **2011**, *19*, 10913−10922.
(22) Antonacci, G.; De Panfilis, S.; Di Domenico, G.; DelRe, E.; Ruocco, G. Breaking the contrast limit in single-pass fabry-pérot spectrometers. *Phys. Rev. Appl.* **2016**, *6*, 054020.
(23) Edrei, E.; Gather, M. C.; Scarcelli, G. Integration of spectral coronagraphy within VIPA-based spectrometers for high extinction Brillouin imaging. *Opt. Express* **2017**, *25*, 6895−6903.
(24) Meng, Z.; Traverso, A. J.; Yakovlev, V. V. Background clean-up in Brillouin microspectroscopy of scattering medium. *Opt. Express* **2014**, *22*, 5410−5415.
(25) Antonacci, G. Dark-field Brillouin microscopy. *Opt. Lett.* **2017**, *42*, 1432−1435.
(26) Antonacci, G.; Lepert, G.; Paterson, C.; Török, P. Elastic suppression in Brillouin imaging by destructive interference. *Appl. Phys. Lett.* **2015**, *107*, 061102.
(27) Fiore, A.; Zhang, J.; Shao, P.; Yun, S. H.; Scarcelli, G. High-extinction virtually imaged phased array-based Brillouin spectroscopy of turbid biological media. *Appl. Phys. Lett.* **2016**, *108*, 203701.
(28) Shao, P.; Besner, S.; Zhang, J.; Scarcelli, G.; Yun, S.-H. Etalon filters for Brillouin microscopy of highly scattering tissues. *Opt. Express* **2016**, *24*, 22232−22238.
(29) Lepert, G.; Gouveia, R. M.; Connon, C. J.; Paterson, C. Assessing corneal biomechanics with Brillouin spectro-microscopy. *Faraday discuss* **2016**, *187*, 415−428.
(30) Bogaerts, W.; De Heyn, P.; Van Vaerenbergh, T.; De Vos, K.; Kumar Selvaraja, S.; Claes, T.; Dumon, P.; Bienstman, P.; Van Thourhout, D.; Baets, R. Silicon microring resonators. *Laser Photonics Rev.* **2012**, *6*, 47−73.
(31) Oda, K.; Takato, N.; Toba, H.; Nosu, K. A wide-band guided-wave periodic multi/demultiplexer with a ring resonator for optical FDM transmission systems. *J. Lightwave Technol.* **1988**, *6*, 1016−1023.
(32) Sun, Y.; Fan, X. Optical ring resonators for biochemical and chemical sensing. *Anal. Bioanal. Chem.* **2011**, *399*, 205−211.
(33) Rahim, A.; Ryckeboer, E.; Subramanian, A. Z.; Clemmen, S.; Kuyken, B.; Dhakal, A.; Raza, A.; Hermans, A.; Muneeb, M.; Dhoore, S.; et al. Expanding the silicon photonics portfolio with silicon nitride photonic integrated circuits. *J. Lightwave Technol.* **2017**, *35*, 639−649.
(34) Dhakal, A.; Subramanian, A. Z.; Wuytens, P.; Peyskens, F.; Le Thomas, N.; Baets, R. Evanescent excitation and collection of spontaneous Raman spectra using silicon nitride nanophotonic waveguides. *Opt. Lett.* **2014**, *39*, 4025−4028.
(35) Antonacci, G.; Goyvaerts, J.; Zhao, H.; Baumgartner, B.; Lendl, B.; Baets, R. Ultra-sensitive refractive index gas sensor with functionalized silicon nitride photonic circuits. *APL photonics* **2020**, *5*, 081301.
(36) Tinguely, J.-C.; Helle, Ø. I.; Ahluwalia, B. S. Silicon nitride waveguide platform for fluorescence microscopy of living cells. *Opt. Express* **2017**, *25*, 27678−27690.
(37) Sui, G.-r.; Chen, B.-x.; Zhou, J.-z.; Fu, C.-s.; Iso, M. Automatic optic waveguide chip packaging system based on center-integration algorithm. *Opt. Commun.* **2008**, *281*, 1515−1521.
(38) Hosseini, E. S.; Yegnanarayanan, S.; Atabaki, A. H.; Soltani, M.; Adibi, A. Systematic design and fabrication of high-Q single-mode pulley-coupled planar silicon nitride microdisk resonators at visible wavelengths. *Opt. Express* **2010**, *18*, 2127−2136.
(39) Lu, X.; Li, Q.; Westly, D. A.; Moille, G.; Singh, A.; Anant, V.; Srinivasan, K. Chip-integrated visible−telecom entangled photon pair source for quantum communication. *Nat. Physics* **2019**, *15*, 373−381.
(40) Doolin, C.; Doolin, P.; Lewis, B.; Davis, J. Refractometric sensing of Li salt with visible-light Si3N4 microdisk resonators. *Appl. Phys. Lett.* **2015**, *106*, 081104.

https://doi.org/10.1021/acsphotonics.2c00005
ACS Photonics 2022, 9, 772−777

(41) Sinclair, M.; Gallacher, K.; Sorel, M.; Bayley, J. C.; McBrearty, E.; Millar, R. W.; Hild, S.; Paul, D. J. 1.4 million Q factor Si 3 N 4 micro-ring resonator at 780 nm wavelength for chip-scale atomic systems. *Opt. Express* **2020**, *28*, 4010−4020.
(42) Stefan, L.; Bernard, M.; Guider, R.; Pucker, G.; Pavesi, L.; Ghulinyan, M. Ultra-high-Q thin-silicon nitride strip-loaded ring resonators. *Opt. Lett.* **2015**, *40*, 3316−3319.
(43) Forrest, J.; Dalnoki-Veress, K.; Dutcher, J. Brillouin light scattering studies of the mechanical properties of thin freely standing polystyrene films. *Phys. Rev. E* **1998**, *58*, 6109.

https://doi.org/10.1021/acsphotonics.2c00005
ACS Photonics 2022, 9, 772−777